Research on the Aerodynamic Characteristics of an Ultrahigh-speed Elevator During the Staggering Process Between the Car and Counterweight

B. Liu[1], J. C. Ma[2], J. Zhang[1†], M. Z. Li[1], Z. X. Tian[1], M. M. Liu[1], H. Zhang[2] and L. Xu[2]

1 Shanghai Ocean University, College of Engineering, Shanghai 201306, China
2 Hitachi Elevator (Shanghai) 2, Co., Ltd., Shanghai, 201700, China

†*Corresponding Author Email: zhangjun@shou.edu.cn*

ABSTRACT

Investigating the aerodynamic characteristics of an ultrahigh-speed elevator between the car and counterweight during the staggering process is crucial for the development of drag reduction and noise abatement technologies. In this study, an actual operating ultrahigh-speed elevator is selected as the research object, and an unsteady flow numerical simulation model for three-dimensional, has been constructed using the method of dynamic mesh. The aerodynamic behaviours of the elevator at various interleaving operating speeds are analysed. The impacts of the counterweight on the flow velocity, pressure, lateral force, aerodynamic drag, and sound pressure level (SPL) of the car are investigated. The results show that a streamlined counterweight can stabilize airflow between the windward areas of the car and counterweight, reducing turbulence, the lateral lift, surface pressure gradients, and SPL, while also lessening the effects of reduced car-counterweight spacing. At a speed of 6 m/s, a bi-arc counterweight with a radius of 250 mm demonstrates superior performance in reducing lateral lift force and aerodynamic drag compared to a traditional rectangular counterweight, with reductions of 12.2% in lateral lift force and 9.3% in aerodynamic drag. Additionally, the simulation and test errors are within 10%, confirming the accuracy of the numerical calculation method.

1. INTRODUCTION

During high-speed elevator operation, various complex structures, including the elevator car, fairing, and accompanying components, rapidly compress, expand, accumulate, or recoil the airflow in the shaft, impacting on the running stability and safety of the elevator. This causes the car to shake persistently and generate intense aerodynamic noise (Park et al., 2019; Okino et al., 2021; Lee et al., 2022). In the interleaving process between the car and counterweight, significant changes in the car's aerodynamic characteristics. These variations result in increased pressure on the guide shoe rollers and a heightened instability and intensification of the sound source, particularly when the elevator car is in high-speed operation (Wang et al., 2014). Exploring the impact factors of the ultrafast elevator car and counterweight's structural parameters and interlacing velocities on aerodynamic properties is crucial for minimizing drag and noise.

A substantial body of research has been undertaken across the globe on the aerodynamic characteristics of ultrahigh-speed elevators. Yang et al. (2004) reported a correlation among aerodynamic noise, pressure loss, and turbulence as airflow moves over a car. Shi et al. (2007) analysed the influence of horizontal gaps and interleaving speeds between the car and counterweight. Li and Wang (2009) investigated how aerodynamic resistance, power consumption, and ventilation openings affect a car's performance. Ling et al. (2015) reported that increasing the fairing height reduces aerodynamic drag. Wang et al. (2015) examined the effect of blockage ratios on aerodynamic performance. Kawamura et al. (2016) studied unsteady airflow during car−counterweight interleaving, suggesting fairing design parameters. Chen et al. (2018) explored the changes in airflow within an elevator shaft and assessed how the motion of the car affected air currents in the event of a fire within a building. Qiao et al. (2019) built a theoretical model to investigate the impact of operating speed, blockage ratio, and ventilation

NOMENCLATURE			
A	surface area of the sound source	F_z	aerodynamic drag force
Δ	filtration scale	P_c	fluctuation pressure on the surface of the car
μ	dynamic viscosity	P_s	sound pressure
ρ	fluid density	p	pressure
τ	delay time	r	distance from the sound source to the far-field receiver
C_0	sound velocity in the far-field	$\overline{S_{ij}}$	stress tensor rate
C_s	Smagorinsky constant	u	flow rate
F_y	lateral lift force		

on induced airflow. Yang et al. (2019) analysed how varying speeds and blockage ratios influence aerodynamic behaviours. Cui et al. (2020) reported that larger blockage ratios increase running resistance and cause stronger airflow disturbances behind a car. Li et al. (2020) constructed a 3D computational model using sliding mesh technology to conduct a comparative study on the airflow phenomena within a tunnel, concentrating on the impacts of a solitary train and dual trains traversing the space. Jing et al. (2021) analysed the impact of various shaft configurations and venting settings on aerodynamic forces and shaft pressures for ultrahigh-speed elevator. Yang et al. (2023) created a multivariate numerical model for elevator systems, validated it with real-world elevator test data, and then analysed how air pressure changes during the elevator's acceleration, constant speed, and deceleration stages. Zhang et al. (2023) analysed changes in aerodynamic resistance and lateral forces at different blockage ratios and distances between the car and counterweight. Zhang et al. (2024a) constructed a bionic fairing model for high-speed elevators by analysing the shape of the boxfish and conducted a comparative analysis of the aerodynamic properties and airspeed under varying parameters. Zeng et al. (2024) analysed how pivotal variables affect the car's aerodynamic properties and the effectiveness of its ventilation system.

In brief, previous studies have largely focused on the impact of various factors such as fairing, toe guards blocking ratio, and the shape and number of ventilation holes on the aerodynamic properties inside the shaft. However, research on the influence of counterweight cross-sectional shapes and their parameters on car aerodynamics characteristics has been relatively limited. This study develops a computational simulation model utilizing dynamic mesh technique and performs experiments to corroborate the method's validity through a comparison with experimental outcomes. First, a 3D numerical model of the elevator is developed using the Large Eddy Simulation (LES) turbulence model coupled with the PISO algorithm. Subsequently, an analysis is conducted on the aerodynamic characteristics throughout the interleaved operation of the car and counterweight. This encompassed an examination of velocity distribution, pressure distribution, aerodynamic drag, and SPL. Finally, the analysis is concentrated on the factors that influenced the car's aerodynamic characteristics, which are influenced by factors such as the counterweight cross-sectional shapes, the counterweight spacing, and the speeds at which they are interleaved. This paper comprehensively analyses the dynamic aerodynamic

characteristics and related influencing factors during the crossing process of a car and counterweight. It offers valuable insights for mitigating aerodynamic drag, lift, and noise in ultrahigh-speed elevators.

2. NUMERICAL CALCULATION MODEL

2.1 Structural Model

The main research is the investigation of the interplay between the car and counterweight. Therefore, the impact of the accompanying cable, car door systems, car frame, and other associated mechanical parts on the airflow around the car is assumed to be minimal. The car is regarded as a sealed rectangular structure, with the chimney effect being disregarded in the study. This conceptual operational model of the elevator, which is limited to the car and counterweight, is illustrated in Fig. 1.
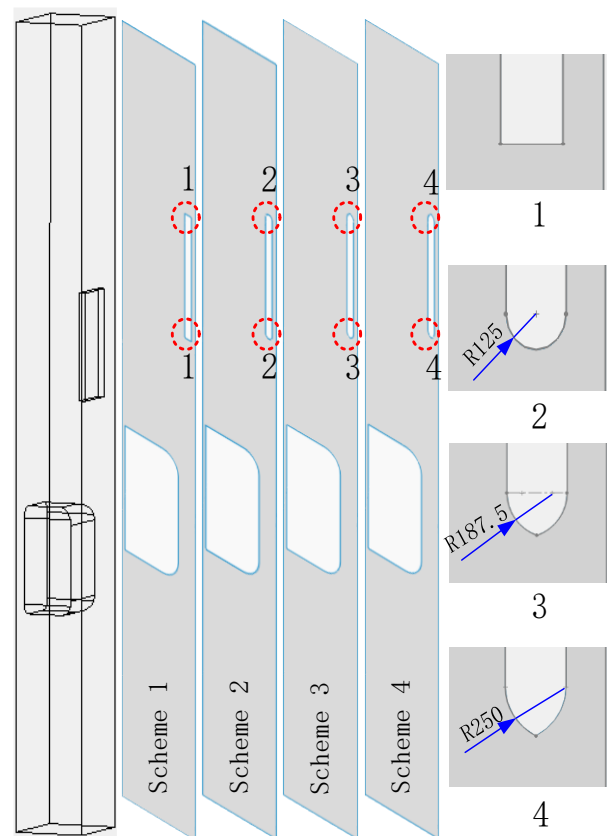
Fig. 1 Simplified model

Table 1 Calculated parameters

parameters	Physical meaning	values (mm)
L_1	The length of the shaft	2800
L_2	The width of the shaft	3100
L_3	The length of the car	2020
L_4	The width of the car	2206
L_5	The width of the counterweight	1800
L_6	The thickness of the counterweight	250
D_1	The distance between the car door side and shaft wall	120
D_2	The distance between the RG side and shaft wall	447
D_3	The distance between the car and the counterweight in three schemes	67, 157, 247
H_1	The height of the car	3700
H_2	The distance between the top of the car and the bottom of the counterweight	14000
H_3	The height of the counterweight	4000
H	The height of the shaft	30000

The aim of this research is to explore the impact of the counterweight's shape on the aerodynamic properties of a car. Four structural design schemes are developed, as shown in Fig. 1. Scheme 1 features a traditional rectangular counterweight with a thickness of 250 mm. Scheme 2 presents a fully arc-shaped counterweight with a radius of 125 mm. Scheme 3 includes a bi-arc counterweight with a radius of 187.5 mm, whereas Scheme 4 consists of a bi-arc counterweight with a radius of 250 mm. The geometrical parameters of the car, counterweight, and shaft are detailed in Table 1. To enable the numerical results of the flow field to be statistically analysed, Fig. 2 presents the monitoring positions on the car. Monitoring plane 1 corresponds to the YOZ plane, and Monitoring plane 2 corresponds to the XOZ plane. Similarly, Monitoring line 1 represents the counterweight side of the car, and Monitoring line 2 represents the roping geared (RG) side. Additionally, four monitoring points are specified within the geometric model.

2.2 Turbulent Model

As the staggering process between the car and counterweight is complicated, the LES model is selected. LES is a specialized filtering technique aimed at accurately resolving motion across all turbulence scales above a certain threshold. This approach captures various unsteady states, large-scale effects, and proposed ordered structures in nonequilibrium processes that surpass the capabilities of the Reynolds-averaged Navier-Stokes approach. Moreover, this method reduces the significant computational burden associated with direct numerical simulation, which requires resolving all turbulence scales. The airflow within the interior of an ultrahigh-speed elevator shaft can be considered a low-velocity incompressible fluid, and its three-dimensional unsteady
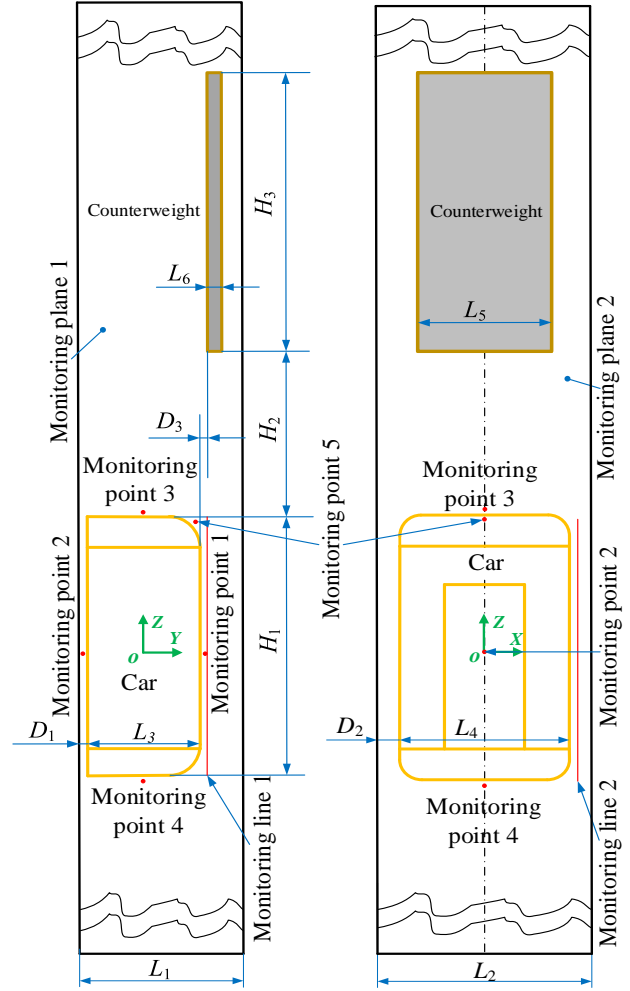
Fig. 2 Monitoring positions

flow process is depicted by LES equations (Hemida & Krajnović, 2010; Cianferra et al., 2019).

$$\frac{\partial \overline{u}_i}{\partial x_i} = 0 \tag{1}$$

$$\frac{\partial \overline{u}_i}{\partial t} + \frac{\partial \overline{u}_i \overline{u}_j}{\partial x_j} = -\frac{1}{\rho}\frac{\partial \overline{p}}{\partial x_i} + \mu \frac{\partial^2 \overline{u}_i}{\partial x_i \partial x_j} - \frac{\partial \overline{\tau}_{ij}}{\partial x_j} \tag{2}$$

where μ and p represent the dynamic viscosity and pressure, respectively; ρ represents the air density; "-" represents the physical spatial filtering process; i and j represent small scales; and u represents the flow rate. Modelling the sub-grid scale stresses as (Zheng et al., 2016):

$$\overline{\tau}_{ij} = 2(C_S \Delta)^2 \overline{S}_{ij}(\overline{S}_{ij}\overline{S}_{ij})^{1/2} - \frac{1}{3}\overline{\tau}_{kk}\delta_{ij} \tag{3}$$

In this context, the filtration scale is represented by the Δ, the sublattice vortex viscosity coefficient is denoted by $\mu_t = (C_S \Delta)^2 \overline{S}_{ij}(\overline{S}_{ij}\overline{S}_{ij})^{1/2}$, the mixing length is indicated by $C_S \Delta$, the Smagorinsky constant is represented by C_S, and the stress tensor rate is expressed
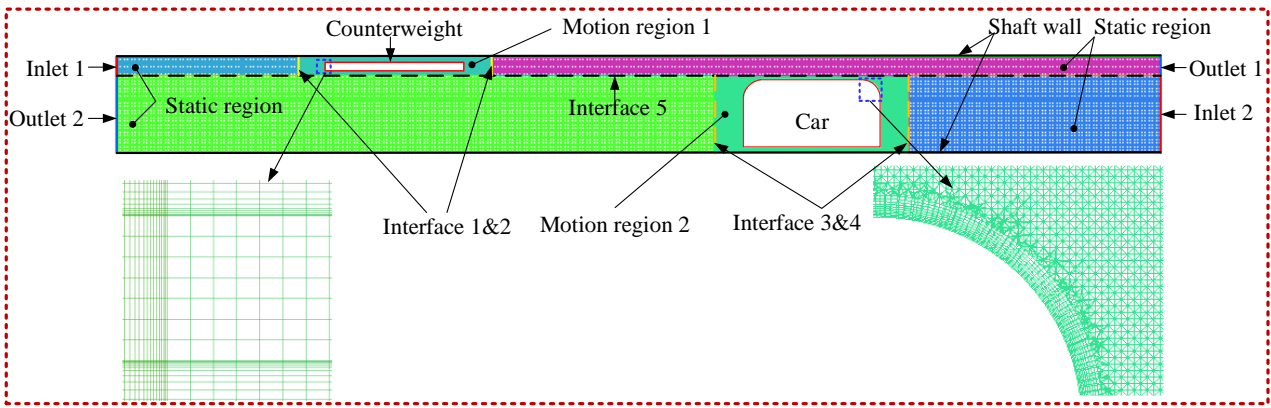
Fig. 3 Hybrid meshing

as $\overline{S}_{ij}$. The following definition is applicable in this instance:

$$\overline{S}_{ij} = \frac{1}{2}\left(\frac{\partial \overline{u}_i}{\partial x_j} + \frac{\partial \overline{u}_j}{\partial x_i}\right) \qquad (4)$$

The near-field noise near the car is solved using Lighthill and Curle acoustic analogy theory. The detailed procedure for determining the acoustic field involves several steps: employing LES to model the time-varying flow field, assessing the fluctuating pressure exerted on the car's surface, transforming the analysis from the time domain to the frequency domain, and ultimately extracting the sonic results. The acoustic equation is articulated below (Ffowcs -Williams & Hawkings, 1969; He et al., 2024):

$$p_s(x,t) = \frac{1}{4\pi c_0}\int_A \frac{\cos\theta}{r}\frac{\partial}{\partial t}P_c(y,\tau)dA(y) \qquad (5)$$

In this context, x is the spatial position vector of the far-field receiver, y is the spatial position vector of the sound source. θ refers to both the normal vector at the sound origin's surface and the angle formed by the vector that extends from the sound origin to the far-field receiver. r signifies the spatial separation between the sound source and the far-field receiver, while τ denotes the delay time.

2.3 Boundary Conditions and Calculation Method

In this study, a numerical simulation of an ultrahigh-speed elevator system has been conducted using ANSYS Fluent to achieve simulation of flow characteristics, a second-order upwind scheme has been implemented. The simulation process used the PISO algorithm, featuring high computational accuracy and stability. This allows for the effective realisation of the synchronous iterative calculation of both the pressure field and the velocity field. To meet the precision of the resulting calculations, we have set the tolerance for data collection to a maximum of 10^{-6}. Figure 3 illustrates that the static pressure of the Inlet 1 and Inlet 2, are set to 0 Pa, respectively. Similarly, the static pressure of the Outlet 1 and Outlet 2, are also defined as 0 Pa. Furthermore, to simulate the effects of the wall, the non-sliding wall boundary conditions are set on the car, counterweight and shaft.

2.4. Grid Independence Verification

Given the operational characteristics of the elevator, the elevator shaft flow field is divided into six computational domains. Specifically, two computational domains encompass the car and counterweight as the movement areas. The external computational domain of the movement area serves as the static area. Additionally, at the boundary between the movement area and the static area, it is necessary to establish an interface through which interactions with the flow field data can occur. Figure 3 presents a local hybrid meshing model of the flow field.

The dynamic mesh method is applicable to the complex phenomenon where the shape of the flow field changes over time due to boundary motion. In this study, this methodology is employed to simulate the staggered motion. A user-defined function (UDF) program defines their motion state, enabling precise control of their relative movement at different speeds. Regarding the dynamic mesh, it is essential to merge and update the mesh of the static region adjacent to the moving region to accommodate the dynamic changes of the boundary. To ensure more accurate control of the grid updating process, a time step of 0.0005 s is set to guarantee the precision and reliability of the simulation.

Four sets of mesh models are established for grid independence verification, with mesh counts of 4.63×10^6, 6.84×10^6, 9.75×10^6, and 14.62×10^6. In the meshing process, it is crucial to determine the appropriate value of y^+. A higher y^+ value is unable to adequately represent the viscous influence region in close to the wall, particularly the attributes of the viscous sublayer and the transition layer. Conversely, a low y^+ value may result in an elevated risk of numerical interpolation errors arising from an excessively dense mesh, potentially compromising the stability and precision of the simulation outcomes. To address this, the first layer of the boundary layer mesh is kept at a thickness of 5 mm, with a growth rate of 1.1, and the mesh count is set to 9.75×10^6, ensuring that y^+ tended to be close to 1. This comprehensive numerical method can effectively capture the flow characteristics in the boundary layer, and the Reynolds number is 3.589×10^5, which is very suitable for describing complex turbulent phenomena at high Reynolds numbers. Table 2 displays the comparison of grid parameters and calculation results.

Table 2 Grid independence validation

Mesh	Number of elements	Number of boundary layers	Average velocity (m/s)	Relative error
Mesh-1	4.63×10^6	5	8.47	4.96%
Mesh-2	6.84×10^6	8	8.28	2.6%
Mesh-3	9.75×10^6	10	8.16	1.1%
Mesh-4	14.62×10^6	14	8.07	-
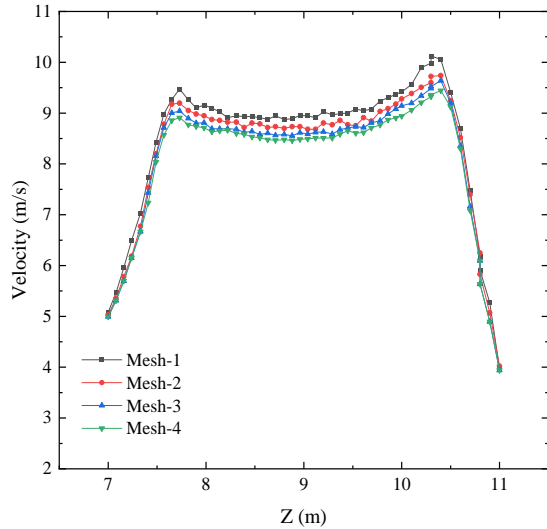
Fig. 4 Velocity at monitoring line 1

Figure 4 shows the velocity profile at Monitoring line 1 when the car is staggered with the counterweight with a velocity of 6 m/s. The velocity curves of the various mesh schemes are similar. The discrepancy in mean velocity between Mesh-1 and Mesh-4 is 4.96%, while the discrepancy from Mesh-2 to Mesh-4 is 2.6% and the discrepancy from Mesh-3 to Mesh-4 is 1.1%. Consequently, to satisfy the demands of calculation accuracy and efficiency, the Mesh-3 scheme is chosen, featuring a total of 9.75×10^6 grids.

2.5 Experimental Verification

The experiment was conducted utilising a TESTO 405i thermal anemometer with the objective of measuring airflow velocity changes over time during elevator operation, thereby validating the numerical calculation methods. Considering the characteristics of the measurement instrument and the constraints of the shaft testing conditions, a measuring point corresponding to Monitoring point 5 has been established on the counterweight side of the car for the purpose of measuring the average air speed. Figure 5 (a) illustrates the measuring range, measuring accuracy, resolution and other parameters of the experimental instrument, which are sufficient to meet the experimental requirements (Zhang et al., 2024b).

The measurement procedures are as follows: First, select the thermal anemometer and adjust the probe direction properly at the test point. Next, as the elevator ascends from the ground floor to the 15th floor, it waits for data stabilization before the test results are output. Finally, the elevator is returned to the ground floor, the steps above are repeated, the results are compared, and the data are filtered to minimize random errors.
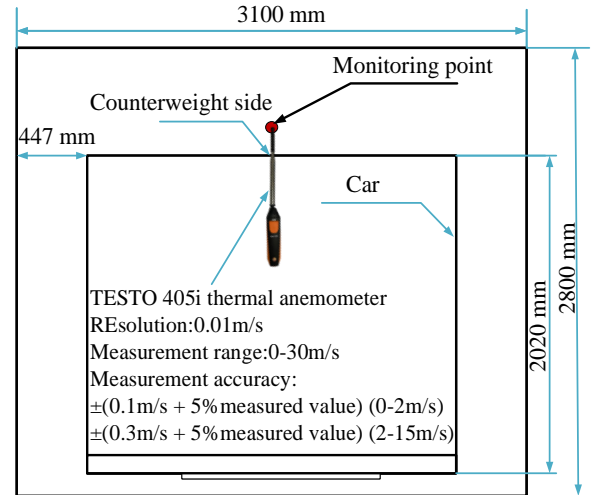
(a) Experimental diagram

(b) Anemometer installation

Fig. 5 Test location

Figure 6 presents a comparative analysis between the numerical simulations and experimental results, illustrating the consistency of trends in wind speed at the monitoring point. Initially, the speed increases uniformly as the elevator accelerates upwards. As the car and counterweight intersect, the anemometer detects a surge in velocity, which is attributed to the unstable airflow resulting from their interaction, followed by a decrease as they separate. The larger deviation between the experimental and simulation results is attributed to airflow obstruction caused by the actual top components of the car.
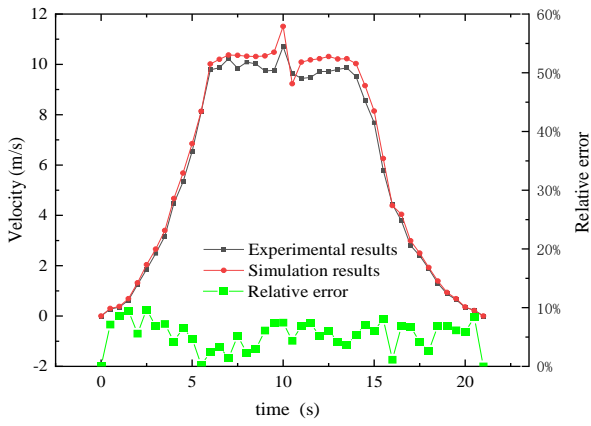
Fig. 6 Comparison between the simulation and experimental results
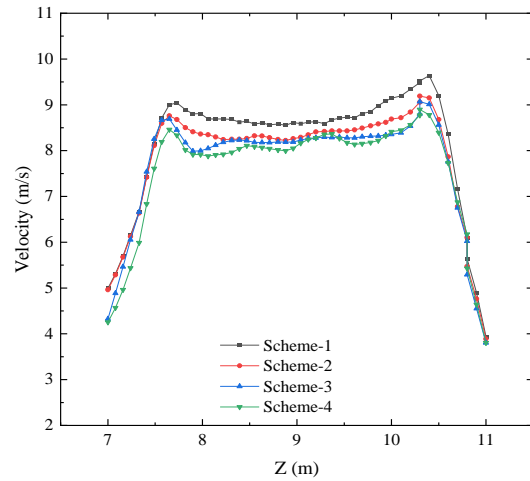
Fig. 7 Velocities on monitoring line 1 at different schemes

Overall, the results obtained from the experimental and simulation work are in general agreement, thereby confirming the precision associated with the numerical calculation techniques employed.

3. CALCULATION RESULTS AND ANALYSIS

3.1 Flow Field Characteristics

Figure 8 displays the velocity contours obtained from Mesh-3 calculations during the staggering process of a car with counterweights of different shapes when $v = 6$ m/s.

The results show that during the car's ascent, high-speed airflow in the annular space flows towards the rear of the car, creating a vortex region at the bottom of the car and deviating towards the side of the car door. This leads to noticeable boundary layer separation and an increased overturning moment. A high-pressure zone forms on the windward side of the car and counterweight, whereas a low-pressure zone and wake flow develop on the leeward side of the counterweight.

(a)　Pre-intersection　　(b)　Intersection　　(c)　Post-intersection
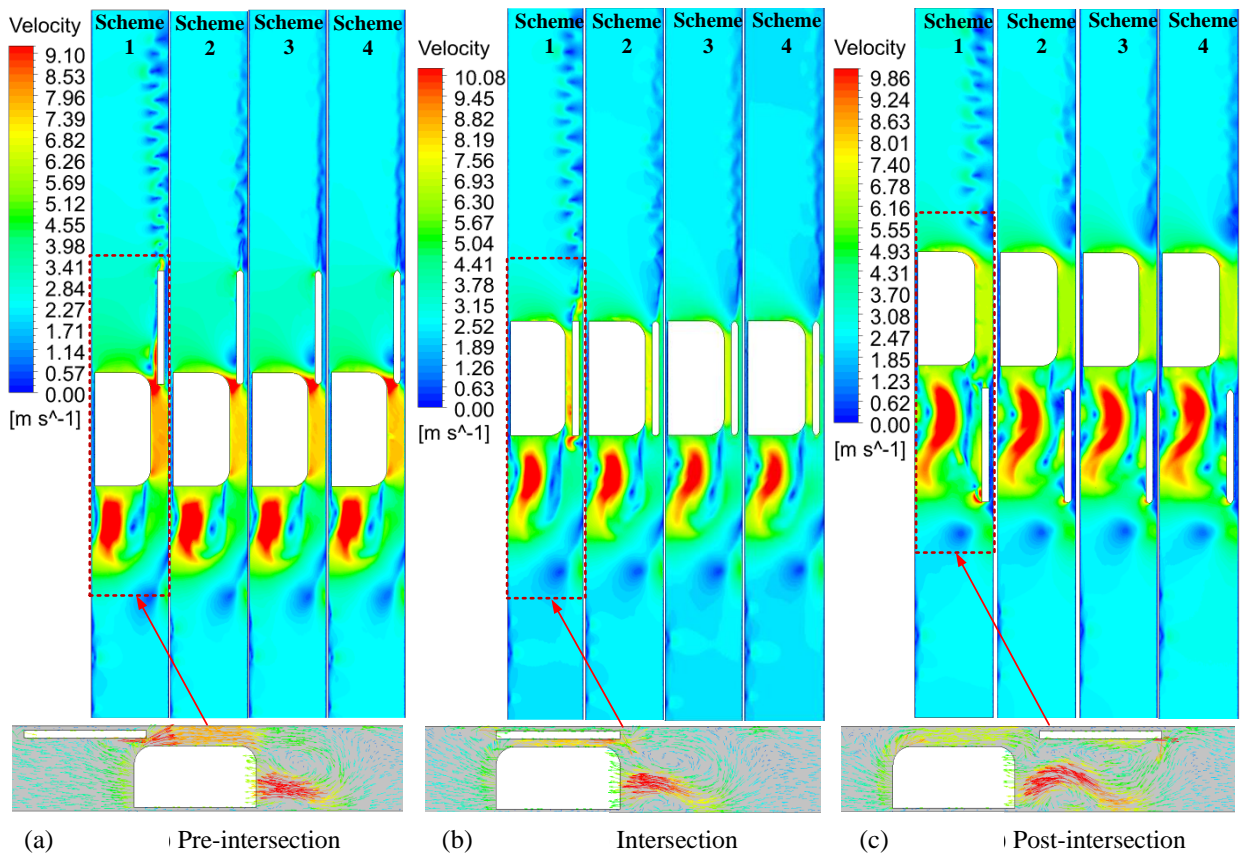
Fig. 8 Velocity contours during the staggering process between the car and the counterweight
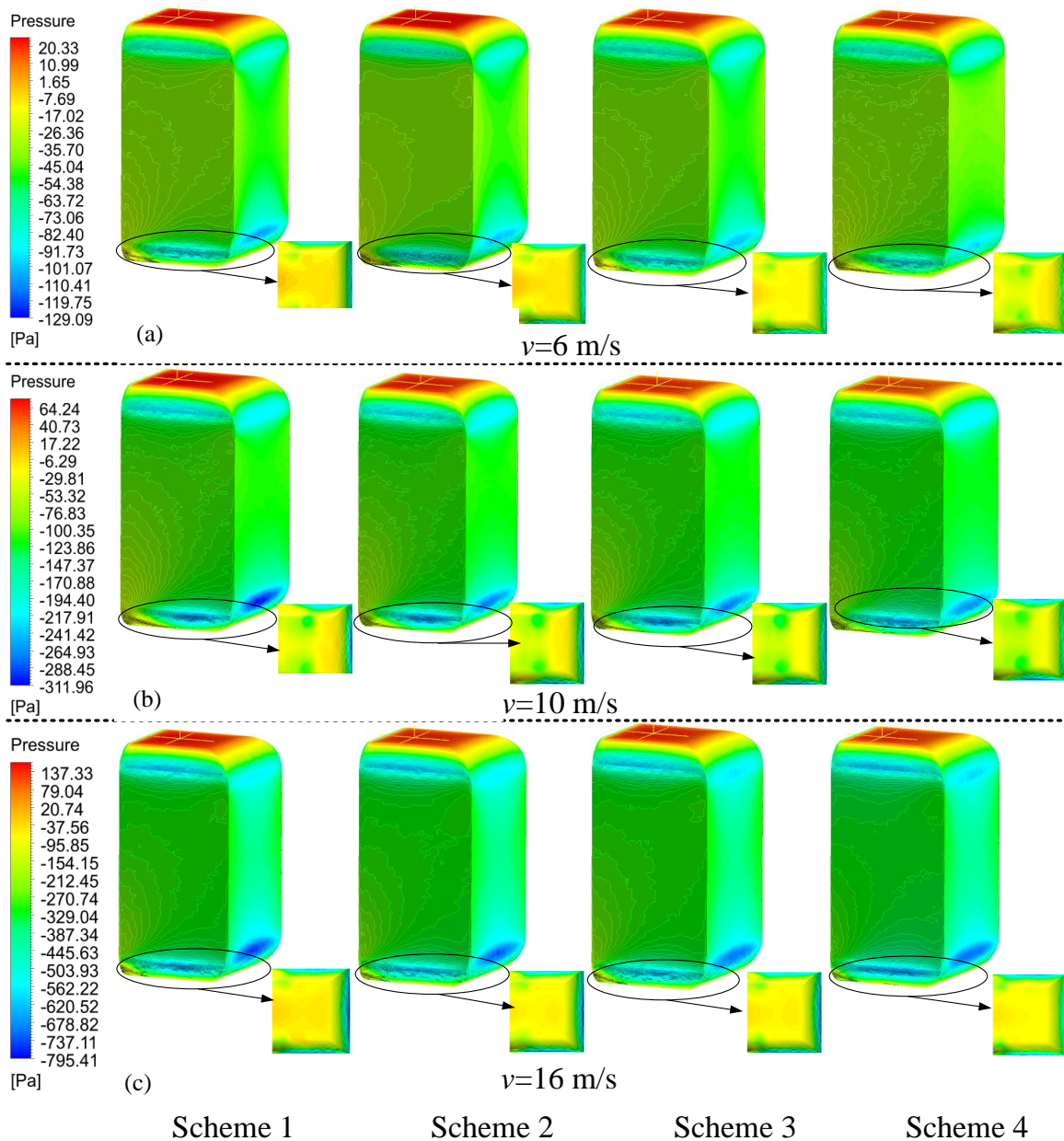
Fig. 9 Pressure contours after the staggering process between the car and the counterweight

Figure 8 (a) shows that the aerodynamic drag on the car increases before it enters the intersection with the counterweight. Among these schemes, Scheme 4 exhibits the smallest high-pressure region on the windward side and the least pronounced wake flow. The velocity vector diagram in Fig. 8 (b) shows that during the intersection, forced airflow from the car's windward side to the counterweight side becomes turbulent because of the counterweight's influence. The shape of the counterweight's cross-section significantly impacts the turbulent velocity. As shown in Fig. 7, Scheme 4 has the smallest velocity variation. Figure 8 (c) shows that as the car and counterweight gradually separate, the interaction between the low-pressure zones on the leeward sides of both creates a deviation in airflow towards the car door side. An increased airflow velocity is observed around the car's underbody and door side. Increasing the counterweight's cross-sectional radius effectively reduces

the airflow velocity in this region, helping to decrease aerodynamic drag.

Figure 9 illustrates the pressure contours on the elevator car after it intersects with the counterweight. The yellow coordinates at the apex of the car represent the pressure maxima, with the coordinates of the maximum pressure point exhibiting minimal variation across the different schemes. The results indicate that the car's pressure distribution is generally consistent, with higher pressure observed towards the windward side and a negation of pressure towards the leeward side. The airflow obstruction is responsible for the high-pressure zone atop the car, whereas the low-pressure zone at the rear, caused by the car's high speed, leads to rapid airflow recirculation. This recirculation is insufficient to compensate for the low-pressure zone created by the car's speed, resulting in differential drag on the car. As shown in Table 3, when different counterweight schemes are

Table 3 Maximum pressure after the staggering process between the car and counterweight occurs

Velocity (m/s)	Scheme 1 (Pa)	Scheme 2 (Pa)	Scheme 3 (Pa)	Scheme 4 (Pa)	Pressure drops (Pa)
6	23.34	21.86	19.52	19.16	17.9%
10	71.83	66.26	61.73	58.21	19%
16	171.73	155.24	149.36	131.94	23.2%

(a) Monitoring line 1, *v*=6 m/s

(b) Monitoring line 2, *v*=6 m/s

(c) Monitoring line 1, *v*=10 m/s

(d) Monitoring line 2, *v*=10 m/s

(e) Monitoring line 1, *v*=16 m/s

(f) Monitoring line 2, *v*=16 m/s
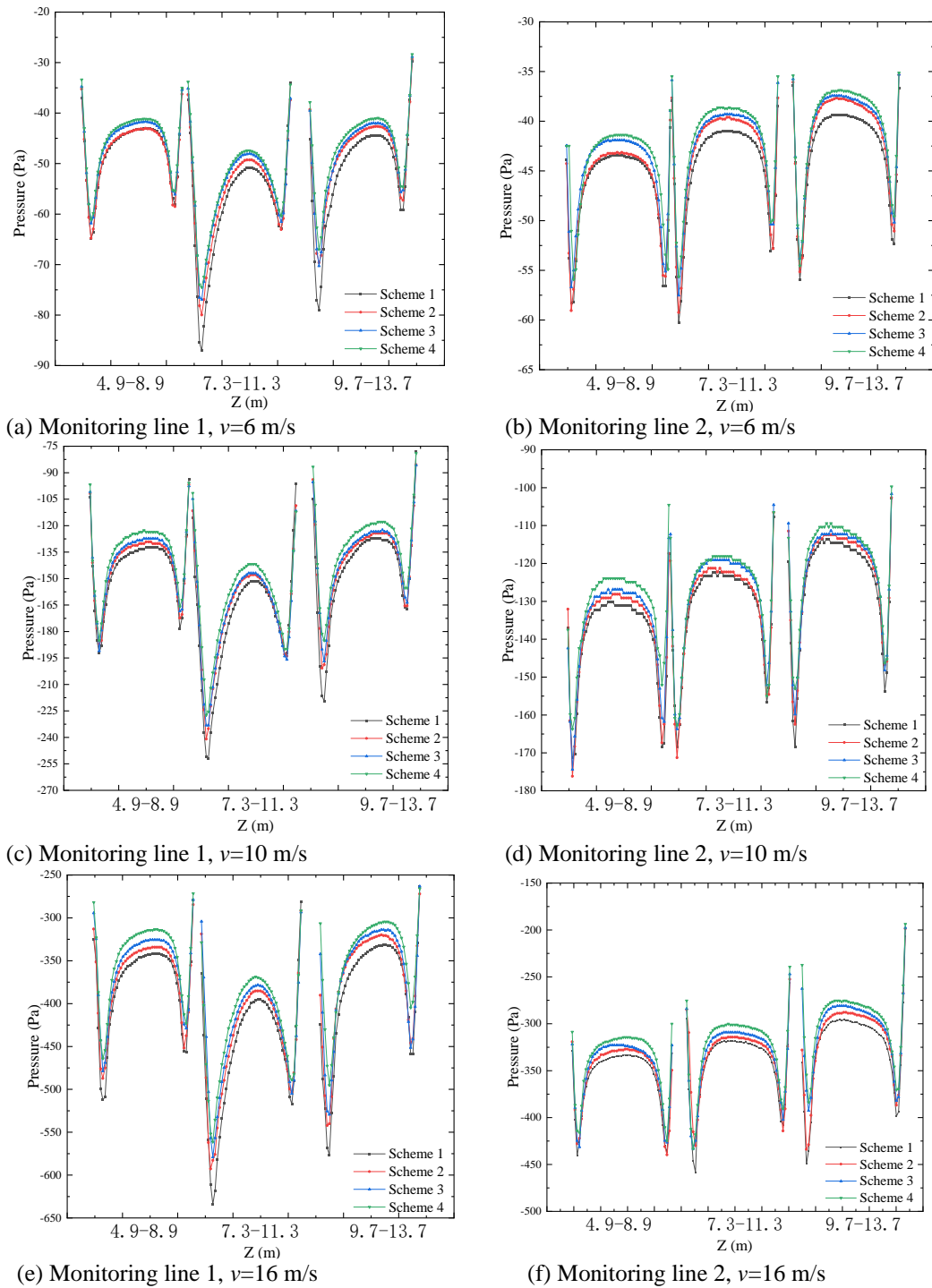
Fig. 10 Pressure curves on different monitoring lines

compared, Schemes 2, 3, and 4 reduce the pressure on the car compared with Scheme 1. At 6 m/s, the results of Scheme 4 indicate a pressure drop of 17.9%. At 10 m/s, the pressure drop is 19%, and at 16 m/s, it is 23.2%.

3.2 Aerodynamic Forces

Figure 10 presents the pressure curves along the surface of the car at three different stages: before, during, and after the intersection with the counterweight. Owing to the forwards motion of the counterweight, airflow
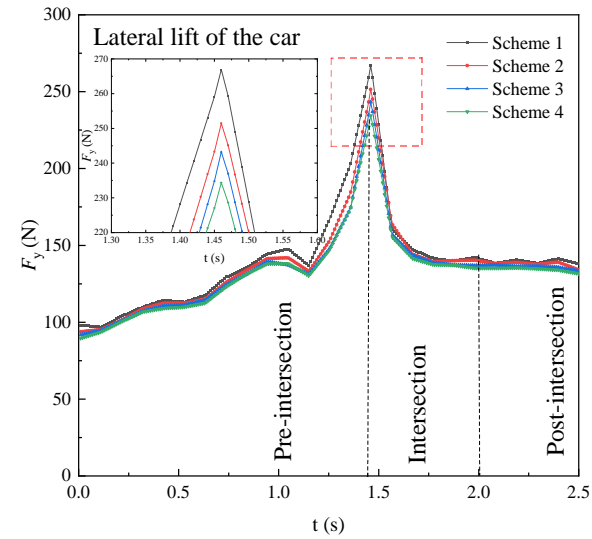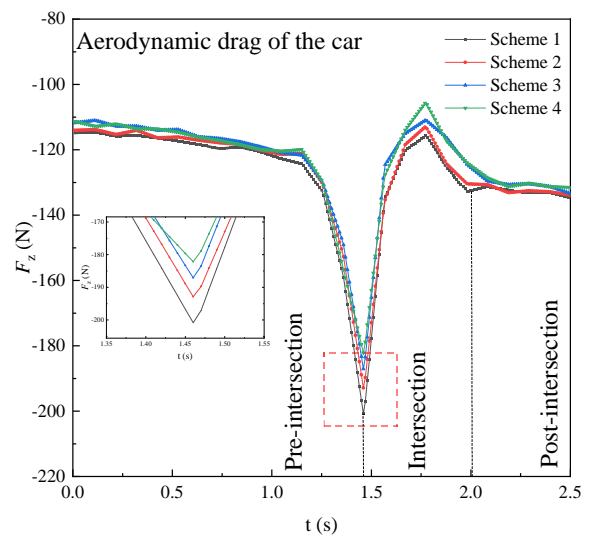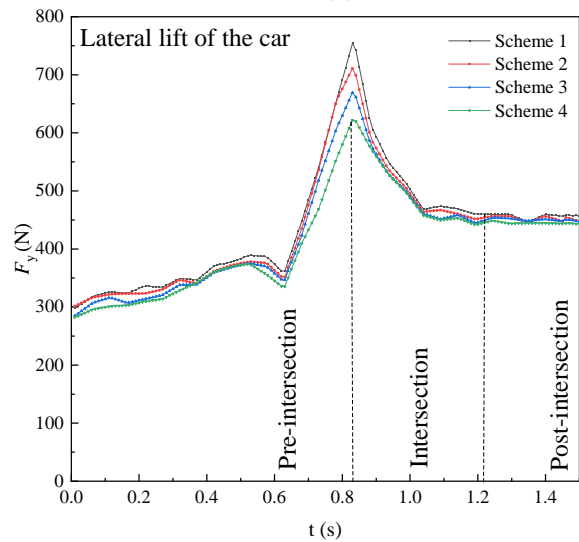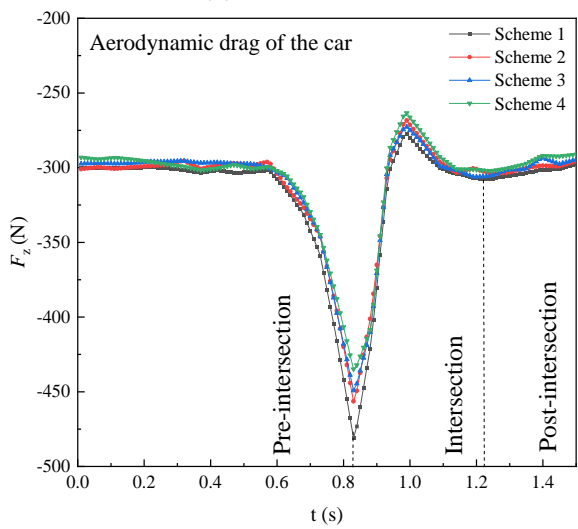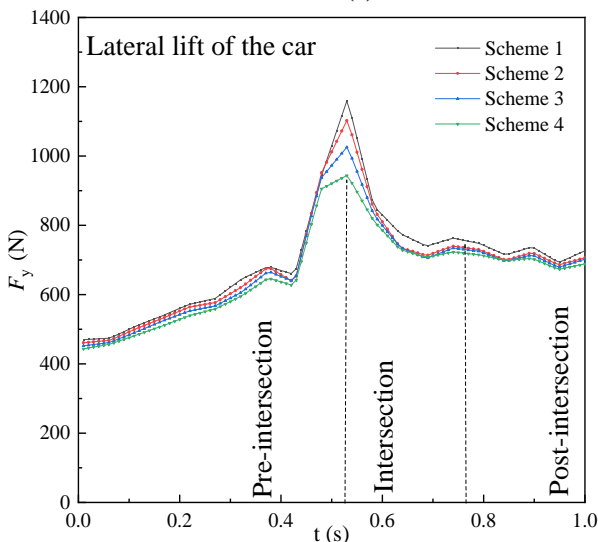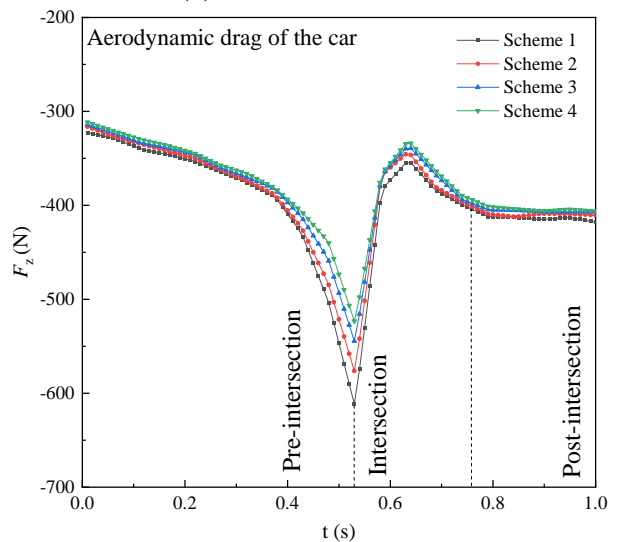
Fig. 11 Aerodynamic forces of the car at different velocities

accelerates from the upper fairing along the car's wall towards the lower fairing. The negative pressure under the

car causes the airflow at the lower fairing to accelerate and move towards the leeward side, contributing to

recirculation. This results in increased pressure at the lower fairing of the car. Across different speeds, the pressure distribution trends before, during, and after the intersection with the counterweight are consistent. The pressure gradually increases from the upper fairing, decreases along the car's wall, and reaches a maximum at the lower fairing. Generally, there is a general tendency for the pressure exerted on the side of the car where the counterweight is located to exceed that exerted on the RG side, which is consistent with the airflow behaviour. Compared with Scheme 1, Schemes 2, 3, and 4 result in lower surface pressures on the car, with Scheme 4 showing the lowest pressure differential. This reduction in pressure helps to decrease the noise generated during the intersection of the elevator.

Figure 11 illustrates the lateral lift force and aerodynamic drag curves of the car throughout its operation. F_y represents the lateral lift, and F_z represents the aerodynamic drag. As the spacing from the car to counterweight decreases, the intensity of the airflow in the windward area of them increases, resulting in more pronounced alterations in the airflow around the car. Before the intersection, the higher speed of the flow on the car's right side, results in the car experiencing positive lift in the Y-axis direction and negative resistance in the Z-axis direction. As the car and counterweight windward areas get closer together, the lift force is reduced and the drag force is increased due to the influence of the counterweight's windward surface on the airflow. During the intersection process, the high airflow velocity between the car and the counterweight reduces the pressure, resulting in a positive lift force along the Y-axis, whereas the negative drag force along the Z-axis reaches its maximum value and then decreases. After the car and counterweight have crossed each other, the lift and drag forces on the car gradually stabilize. A comparison of the maximum lateral lift and drag of the different schemes

reveals that Scheme 4 is the most effective. Figure 12 shows the maximum lateral lift and drag force of the car in the different schemes. Table 4 illustrates that, at 6 m/s, the lateral lift force of Scheme 4 is 12.2% lower than that of Scheme 1. At 10 m/s, a reduction in the lateral lift force of 17.5%, and at 16 m/s, it is reduced by 18.5%. Similarly, at 6 m/s, the aerodynamic drag of Scheme 4 is reduced by 9.3% compared with that of Scheme 1; at 10 m/s, the drag decreases by 9.5%, and at 16 m/s, it is reduced by 14.4%.

Figure 13 illustrates the curves of the lateral lift and aerodynamic drag on the counterweight at different stages. F_{y1} represents the lateral lift force, and F_{z1} represents the aerodynamic drag force. Prior to the intersection, the counterweight experiences the impact of airflow from the car's windward side as their separation decreases, resulting in a positive lift force along the Y-axis and positive resistance along the Z-axis, with both forces continuously increasing. During the intersection process, the negative pressure between the car and the counterweight leads to a negative lift force along the Y-axis and negative resistance in the Z-direction for the counterweight. After the car and counterweight intersect, the lift and resistance forces on the counterweight gradually stabilize. Comparing the maximum lateral lift and aerodynamic resistance of the different schemes demonstrates that Scheme 4 has been demonstrated to be the most successful in terms of the reduction of lift force. Figure 14 shows the maximum lateral lift and drag force of the counterweight in the different schemes. Table 5 illustrates that, at 6 m/s, the lateral lift force of Scheme 4 is 12.2% lower than that of Scheme 1. At 10 m/s, a reduction in the lateral lift force of 17.5%, and at 16 m/s, it is reduced by 18.5%. Similarly, at 6 m/s, the aerodynamic drag of Scheme 4 is reduced by16.7% compared with that of Scheme 1; at 10 m/s, the drag decreases by 21.7%, and at 16 m/s, it is reduced by 17.8%.
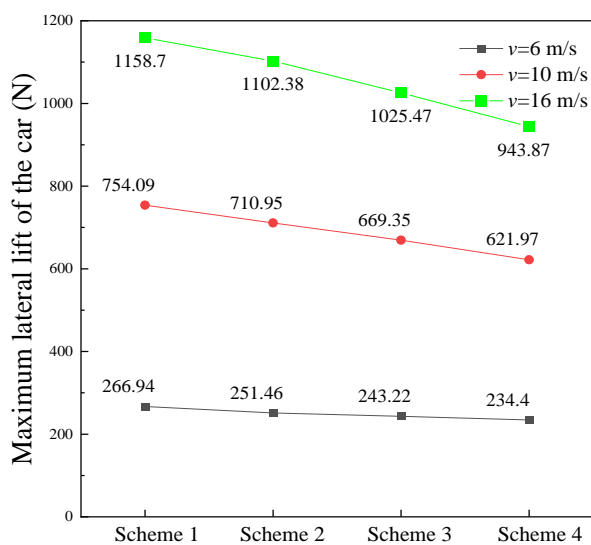
(a) Lateral lift
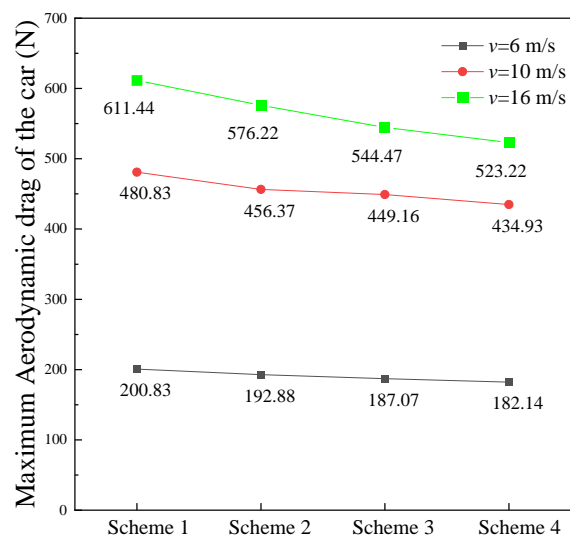
(b) Aerodynamic drag

Fig. 12 Maximum aerodynamic forces of the car at different schemes

Table 4 Reduction in aerodynamic forces of the car in different schemes compared to Scheme 1

v (m/s)	Lateral lift			Aerodynamic drag		
	Scheme 2	Scheme 3	Scheme 4	Scheme 2	Scheme 3	Scheme 4
6	5.8%	8.9%	12.2%	4%	6.9%	9.3%
10	5.7%	11.2%	17.5%	5.1%	6.6%	9.5%
16	4.9%	11.5%	18.5%	5.8%	11%	14.4%
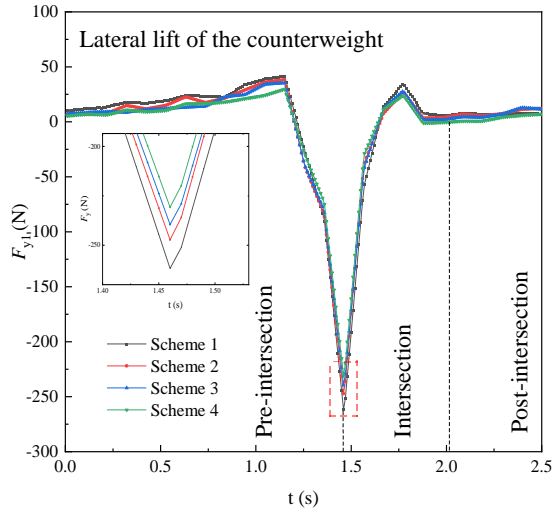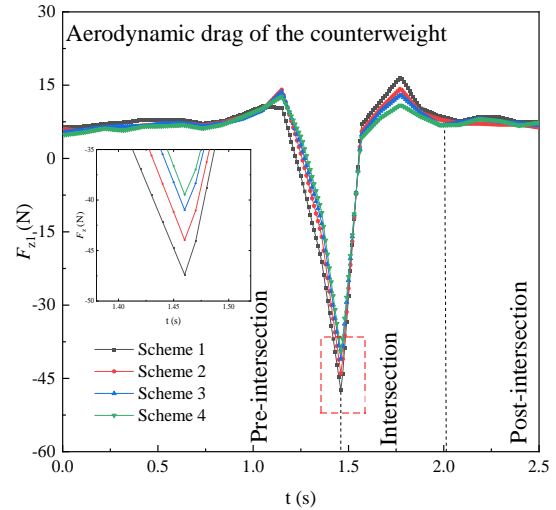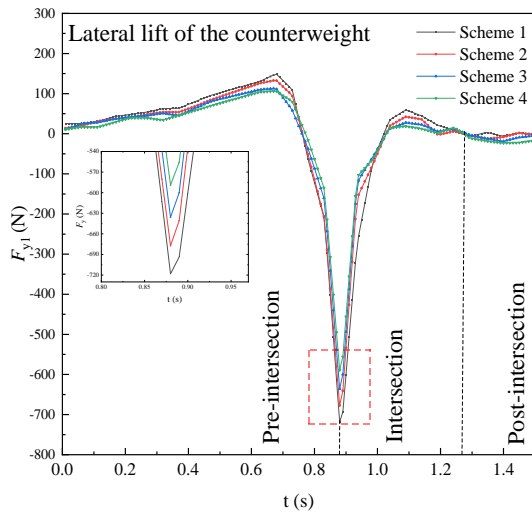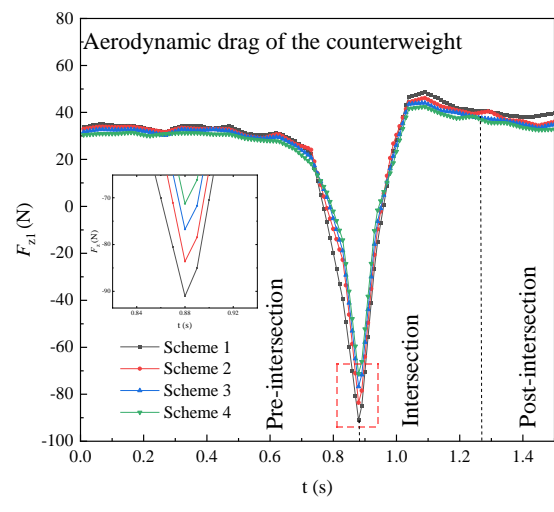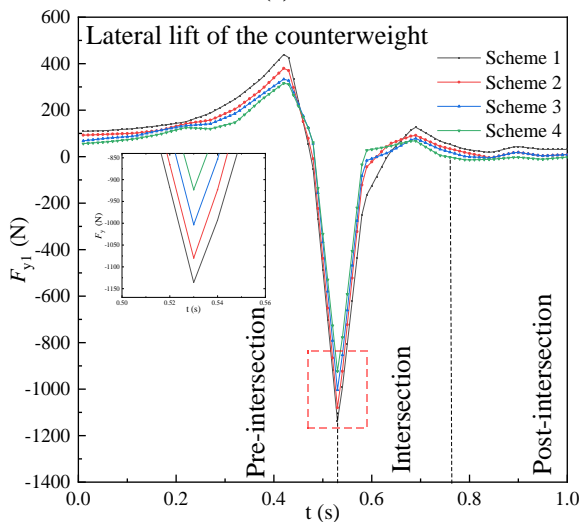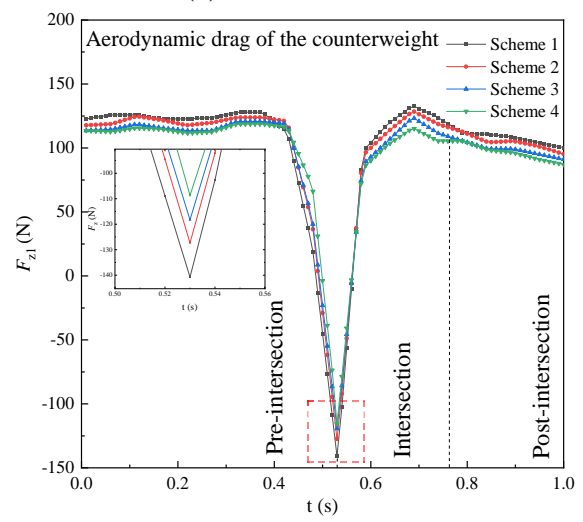
Fig. 13 Aerodynamic forces of the counterweight at different velocities

(a) Lateral lift
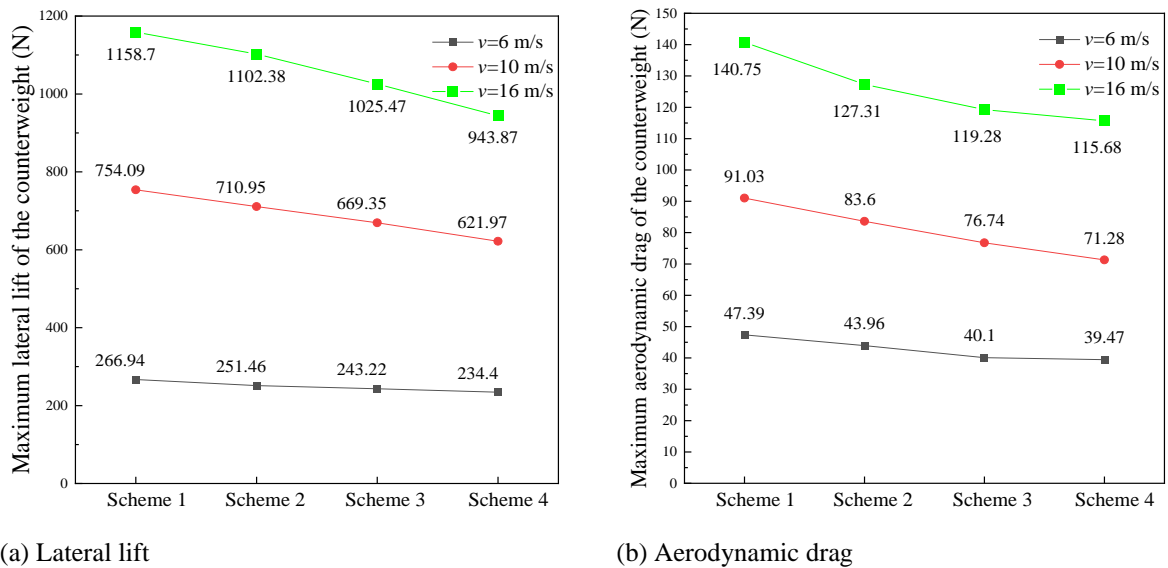
(b) Aerodynamic drag

Fig. 14 Maximum aerodynamic forces of the counterweight at different schemes

Table 5 Reduction in aerodynamic forces of the counterweight in different schemes compared to Scheme 1

v (m/s)	Lateral lift			Aerodynamic drag		
	Scheme 2	Scheme 3	Scheme 4	Scheme 2	Scheme 3	Scheme 4
6	5.8%	8.9%	12.2%	7.2%	15.4%	16.7%
10	5.7%	11.2%	17.5%	8.2%	15.7%	21.7%
16	4.9%	11.5%	18.5%	9.5%	15.3%	17.8%

3.3 Aerodynamic Acoustic

Figure 15 illustrates the sound pressure level surrounding the car at various monitoring points in different counterweight configurations and at various speeds. Notably, the noise spectra at identical monitoring points across different counterweight schemes are largely consistent, with no distinct peaks being evident across the entire frequency spectrum, classifying the noise as broadband in nature. Among the schemes, Scheme 4 results in the lowest sound pressure levels, whereas Scheme 1 results in the highest. This disparity is attributed to the larger eddy currents generated in the windward area of the counterweight in Scheme 1, which exert a more pronounced influence on the car's vicinity. Monitoring point 2, situated adjacent to the car door, is minimally influenced by the variations in the counterweight schemes in terms of the sound pressure level. The monitoring point on the car's counterweight side experiences significant variations in sound pressure level due to alterations in the counterweight scheme, as this region is directly affected by the flow from the counterweight. With increasing velocity, the trend of the noise spectrum of each monitoring point remained basically unchanged, but the sound pressure level increased significantly. Across the spectrum of speeds, Scheme 4 consistently has the lowest noise levels, which is advantageous for mitigating noise pollution.

3.4 Different Car Counterweight Spacing

A comparative analysis of various counterweight schemes reveals that Scheme 4 offers a notably greater reduction in lateral lift force as the velocities of both the car and counterweight increase. To further investigate the impact of Scheme 4 on the car, various counterweight spacings were analysed for an elevator operating at a rated speed of 16 m/s. According to elevator manufacturing and safety standards, the distance between the car and its associated components and between the counterweight and its components should not be less than 50 mm. Therefore, car counterweight spacings D_3 of 67 mm, 157 mm, and 247 mm were selected for analysis.

Figure 16 displays the velocity distribution contours for three different counterweight spacings at three operational stages. The trends of the velocity contours for the different counterweight spacings are generally consistent. During the staggering process, the velocity reaches its maximum. After the intersection, as the car and counterweight separate, their mutual influence diminishes, causing the velocity to decrease. The peak speed occurs at the bottom of the car, close to the car door. For D_3=67, the maximum velocity is 23.58 m/s; for D_3=157, the maximum velocity is 22.46 m/s; and for D_3=247, the maximum velocity is 21.97 m/s. With decreasing counterweight spacing, the size of the car's bottom separation vortex expands, leading to higher flow speeds at the car's bottom. Using the two-sided arc-shaped counterweight in Scheme 4 helps reduce the impact on the airflow velocity. Fig. 17 shows the pressure curves for different monitoring lines after the intersection. The pressure curves for the three different counterweight spacings exhibit similar trends, with higher pressures observed at the upper and lower fairings of the car. As the counterweight spacing decreases, airflow speed increases at the intersection of the car and counterweight, leading to

(a) Monitoring point 1

(b) Monitoring point 2

(c) Monitoring point 3

(d) Monitoring point 4
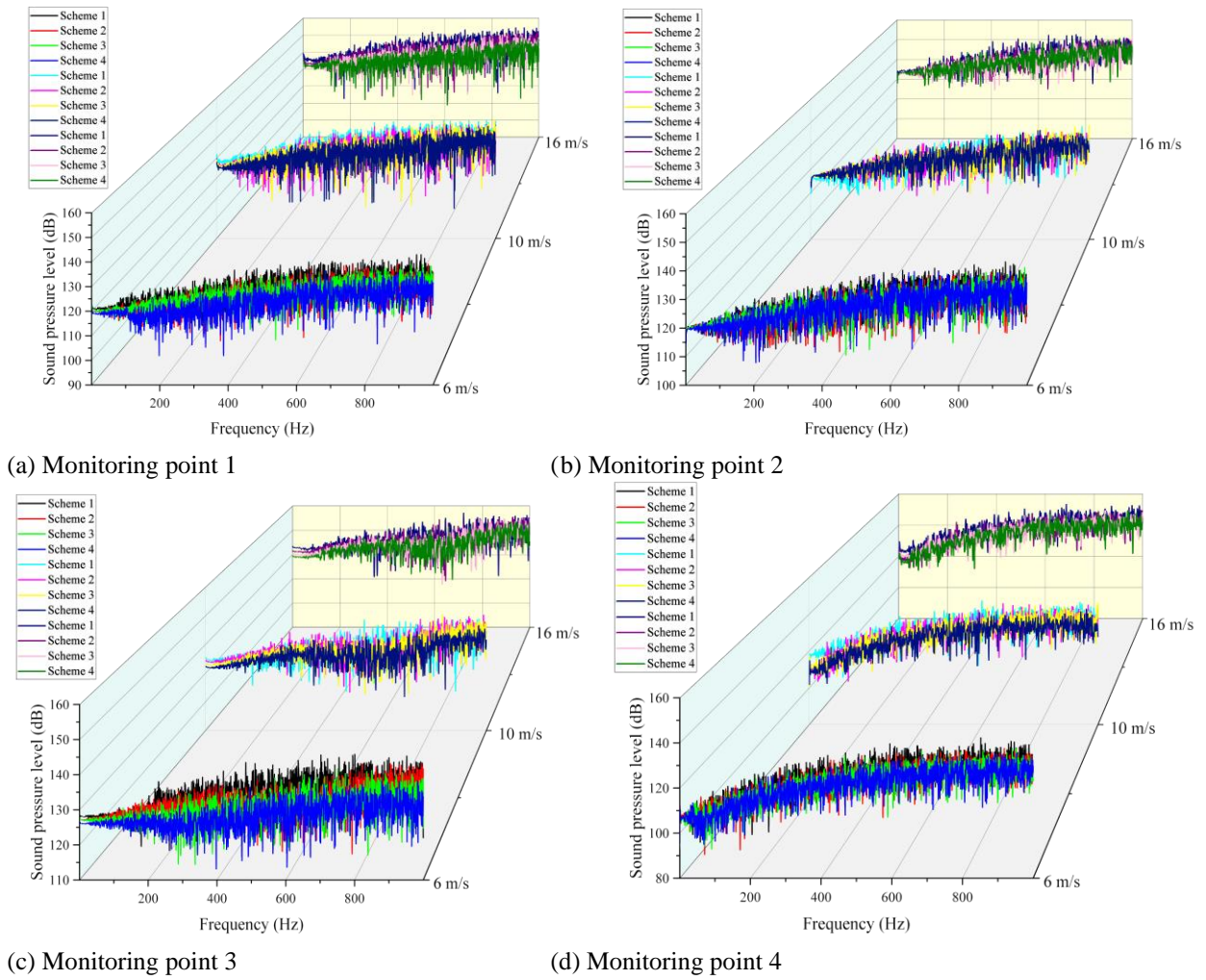
Fig. 15 Noise spectra at different monitoring points

(a) Pre-intersection

(b) Intersection

(c) Post-intersection
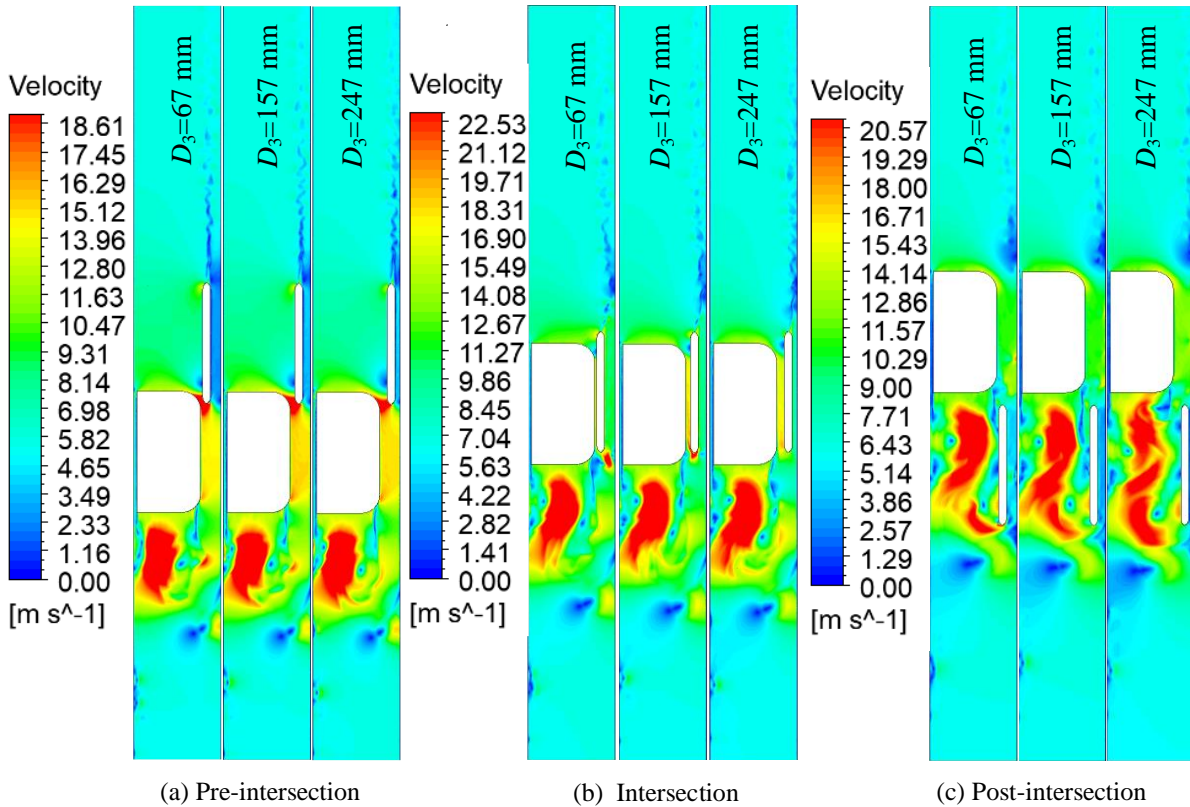
Fig. 16 Velocity contours at different spacings between the car and the counterweight (*v*=16 m/s)

(a) Monitoring line 1　　　　　　　　　　(b) Monitoring line 2
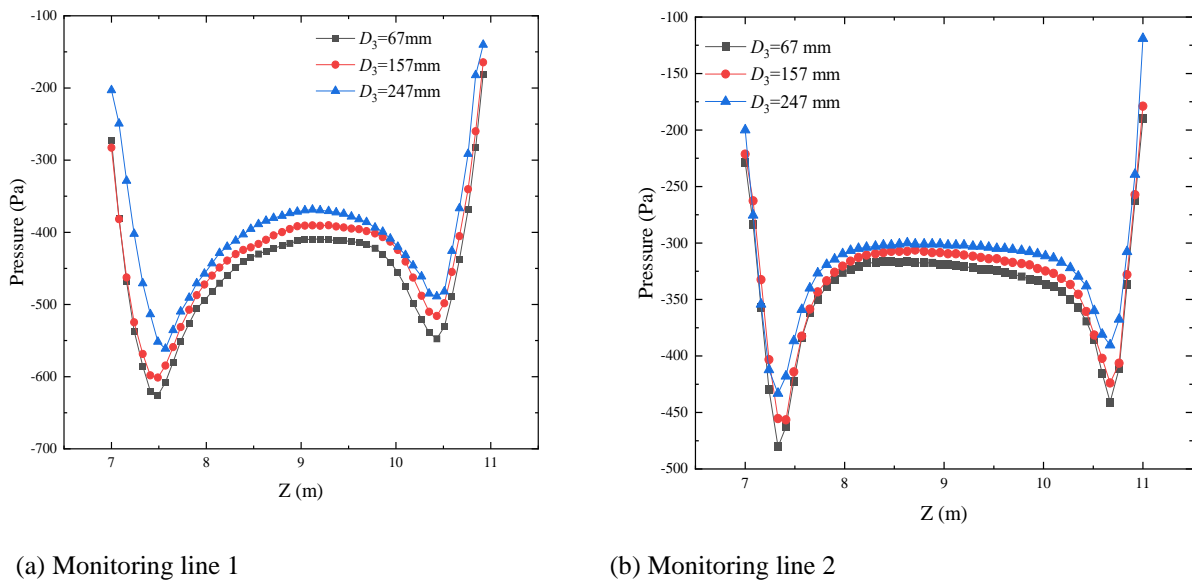
Fig. 17 Pressure curves during the staggering process (v=16 m/s)

a greater pressure difference and increased pressure on the car. Employing the double-sided arc-shaped counterweight in Scheme 4 helps mitigate the effects of reduced counterweight spacing on the car.

4. CONCLUSION

In this research, a three-dimensional unsteady flow field numerical model for ultrahigh-speed elevators was developed. Based on grid independence tests and validation of the computational methods, the influences of the counterweight cross-sectional shape, counterweight spacing, and intersection speed on the velocity distribution in the flow field, pressure on the car surface, aerodynamic force and SPL were explored. The major conclusions are presented here:

(1) Before the intersection of the car and the counterweight, as they get closer, the airflow accelerates along the car's wall towards the bottom, causing significant changes in surface pressure and an increase in aerodynamic forces exerted on the car. Among the various schemes, the two-sided arc-shaped counterweight effectively reduces the pressure difference, the lateral lift force, and the aerodynamic drag during the intersection. Moreover, more pronounced drag and noise reduction effects are observed at higher speeds.

(2) The counterweight with arc-shaped cross-sections markedly enhances the streamlining effect in the windward area, reducing the airflow interaction in the windward zones around the car and the counterweight. This leads to a decrease in the airflow towards the car's leeward area and reduces the size of the vortex detached on the car's leeward side.

(3) As the counterweight spacing decreases, an increase is noted in the velocity of the airflow between them. Consequently, this gives rise to an increase in negative pressure and makes the vortex in the lower leeward area of the car more turbulent and disordered.

This results in an enlarged vortex area and increased flow speed at the car's bottom. The two-sided arc-shaped counterweight reduces the impact on the surrounding airflow speed and wall pressure, thereby minimizing the aerodynamic forces and noise generated during the intersection.

(4) During the staggering motion of the elevator, the SPL on the car's surface shows no peak and the noise is of broadband nature. Changes in the counterweight configuration significantly influence the SPL at the monitoring point on the car's counterweight side. As the velocity increases, the SPL trends at each monitoring point remain largely consistent, while there is a notable increase in the SPL. Throughout the range of speeds, Scheme 4 consistently has the lowest noise levels, which is beneficial for reducing noise pollution.

(5) When the elevator descends along the vertical shaft, the aerodynamic characteristics of the elevator system undergo alterations. The windward and leeward areas switch positions compared to when the elevator is ascending. This transformation is driven by the dynamic airflow created due to the elevator's movement within the shaft. The underside of the car becomes the windward side, generating a high-pressure area during descent. The changes in the windward and leeward aspects also imply corresponding variations in the aerodynamic drag experienced by the car and counterweight.

CONFLICT OF INTEREST

No potential conflicts of interest were reported by the authors.

AUTHOR CONTRIBUTION

Bei Liu ： Conceptualization, Writing – original draft，Software. **Jiancheng Ma:** Validation, Resources, Supervision. **Jun Zhang:** Formal analysis, Writing – review & editing, Funding acquisition. **Minzong Li:** Investigation. **Manman Liu:** Software. **Zhongxu Tian:** Supervision. **Hong Zhang:** Investigation. Lei Xu: Data curation.

REFERENCES

Chen, Y. Q., Yang, L. Z., Fu, Z. J., Chen, L. F., & Chen, J. M. (2018). Gas flow behavior and flow transition in elevator shafts considering elevator motion during a building fire. *Building Simulation*, *11*(4), 765-771. https://doi.org/10.1007/s12273-018-0430-3

Cianferra, M., Ianniello, S., & Armenio, V. (2019). Assessment of methodologies for the solution of the Ffowcs Williams and Hawkings equation using LES of incompressible single-phase flow around a finite-size square cylinder. *Journal of Sound and Vibration*, *453*, 1–24. https://doi.org/10.1016/j.jsv.2019.04.001.

Cui, H. W., Zhang, Q., Zhang, R. J., & Zhang, L. Z. (2020). Research on aerodynamic and flow field characteristics of high speed elevator with different shaft blockage ratio. *Journal of Physics: Conference Series*, *1653*(1), 012024-012024. https://doi.org/10.1088/1742-6596/1653/1/012024

Ffowcs-Williams, J, E., & Hawkings, D. L. (1969). Sound generation by turbulence and surfaces in arbitrary motion. *Philosophical Transactions of the Royal Society of London. Series A, Mathematical and Physical Sciences.* 264321–342. http://doi.org/10.1098/rsta.1969.0031

He, Q., Yang, G. F., Zhang, R. J., Zhang, C. L., & Ma, K. (2024). Research on the unsteady flow field and aerodynamic noise characteristics in the circular space of ultra-high-speed elevators. *Physics of Fluids*, *36*(5), 055103. https://doi.org/10.1063/5.0 206516

Hemida, H., & Krajnović, S. (2010). LES study of the influence of the nose shape and yaw angles on flow structures around trains. *Journal of Wind Engineering and Industrial Aerodynamics*, *98*(1), 0167-6105. https://doi.org/10.1016/j.jweia.2009.0 8.012

Jing, H., Zhang, Q., Zhang, R. J., & Qin, H. (2021). Aerodynamic characteristics analysis of ultra-high-speed elevator with different hoistway structures. *International Journal of Structural Stability and Dynamics*, *22*(02). https://doi.org/10.1142/s02 19455422500201

Kawamura, Y., Watanabe, T., Kawabata, R., Miyoshi, R., & Miyata, K. (2016). 103 Aerodynamic force suppression method for passing the counter weight in the ultra-high speed elevator. https://doi.org/10.1299/jsmeearc.2016.9

Lee, D. S., Ji, K. H., Jing, J. J., & Jo, J. H. (2022). Experimental study on elevator door reopening

problems caused by stack induced pressure differences across the elevator door in buildings. *Building and Environment*, 0360-1323. https://doi.org/10.1016/j.buildenv.2022.109271

Li, W. H., Liu, T. H., Chen, Z. W., Guo, Z. J., & Huo, X. S. (2020). Comparative study on the unsteady slipstream induced by a single train and two trains passing each other in a tunnel. *Journal of Wind Engineering and Industrial Aerodynamics*, 0167-6105. https://doi.org/10.1016/j.jweia.2020.104095

Li, X. D., & Wang, K. (2009). Optimization of aerodynamic characteristics of high-speed elevator. *Journal of Harbin Institute of Technology*, *41*(6), 82-86. https://doi.org/10.3321/j.issn:0367-6234.2009.0 6.017

Ling, Z. W., Tang, P., Wang, X. B., Lin, Z., & Tang, D. (2015). Research on the drags of high speed elevator with different height diversion cover. Proceedings of the 4th International Conference on Mechatronics, Materials, *Chemistry and Computer Engineering*, 2352-538X. https://doi.org/10.2991/ icmmcce-15.2015.453

Okino, T., Yamagiwa, Y., Arita, S., Ishikawa, Y., & Otsuka, K. (2021). Three-dimensional analysis of a counterweight type space elevator. *Acta Astronautica*, 132-139. https://doi.org/10.1016/j.actaastro.2021.04. 040.

Park, Y., Na, J., Sung, K. H., & Ryou, H. S. (2019). Numerical study on the effect of elevator movement on pressure difference between vestibule and living room in high-rise buildings. *Building Simulation, 12*, 313–321. https://doi.org/10.1007/s12273-018-0477-1.

Qiao, S., Zhang, R. J., He, Q., & Zhang, L. Z. (2019). Theoretical modeling and sensitivity analysis of the car-induced unsteady airflow in super high-speed elevator. *Journal of Wind Engineering and Industrial Aerodynamics*, *188*, 280-93. https://doi.org/10.1016/j.jweia.2019.02.012

Shi, L. Q., Liu, Y. Z., Jin, S. Y., & Cao, Z. M. (2007) Numerical simulation of unsteady turbulent flow induced by two-dimensional elevator car and counter weight system. *Journal of Hydrodynamics*, *19*(6), 720-5. https://doi.org/10.1016/s1001-6058 (08)60009-8

Wang, X. B., Lin, Z., Tang, P., & Ling, Z. W. (2015). *Research of the blockage ratio on the aerodynamic performances of high speed elevator.* International Conference on Mechatronics. https://doi.org/10.299 1/icmmcce-15.2015.451

Wang, X. W., Yu, Y. J., Zhang, R. J., Wang, S. C., & Tian, Y. (2014). Summary of the noise research of high-speed traction elevators. *Noise and Vibration Control*, *34*(03), 1-5. https://doi.org/10.3969/j.issn.1006-1335.2014.03.001

Yang, G. F., He, Q., Li, H., & Li, L. (2023). Analysis of the aerodynamic characteristics of the entire operation process of an ultra-high-speed elevator under the influence of high blockage ratio, hoistway,

and car height parameters. *Physics of Fluids*, *35*(7), 075107. https://doi.org/10.1063/5.0153577

Yang, H. Y., Yang, J., & Xu, B. (2004). Computational simulation and experimental research on speed control of VVVF hydraulic elevator. *Control Engineering Practice*, (12), 563-568. https://doi.org/10.1016/S0967-0661(03)00139-4

Yang, Z., Zhang, Q., & Zhang, R. J. (2019). Study on aerodynamic characteristics of super high-speed elevator. *IOP Conference Series: Materials Science and Engineering*, *583*(1), 012028. https://doi.org/10.1088/1757-899x/538/1/012028

Zeng, X, R., He, Q., Zhang, R, J., Cong, D. S., & Wang D. Q. (2024). Study on the aerodynamic characteristics and ventilation effects of ultra-high-speed elevator car-counterweight system under the influence of multiple parameters. *Physics of Fluids*, *36*(5), 055140. https://doi.org/10.1063/5.0203 953

Zhang, Q., Huang, W. Q., Liu, Q. J., Zhu, X.S., & Zhao, C. (2024a). Research on aerodynamic characteristics of high-speed elevator guide vanes based on box

pufferfish biomimetic drag reduction. *Physics of Fluids*, *36*(7). https://doi.org/10.1063/5.0211794

Zhang, J., Liu, M. M., Li, M. Z., Liu, B., Jin, S. X., Qin, L., Ma, J. C., Zhang, H., & Xu, L. (2024b). Simulation and experimental study on the aerodynamic characteristics of a high-speed elevator with three-sided arc fairings. *Journal of Building Engineering, 81*, 108172-108172. https://doi.org/10.1016/j.jobe.2023.108172

Zhang, X., Zhang, R. J., Jing, H., & He, Q. (2023). Study on aerodynamic characteristics and parameters of high-speed elevator car-counterweight intersection. *Mechanics Based Design of Structures and Machines*, *52*(7), 3750–3774. https://doi.org/10.1080/15397734.2023.2208656

Zheng, W. L., Yan, C., Liu, H. K., & Luo, D. H. (2016). Comparative assessment of SAS and DES turbulence modeling for massively separated flows. *Acta Mechanica Sinica*, *32*(1), 12–21. https://doi.org/10.1007/s10409-015-0505-7